Shape and Tip Force Estimation of Concentric Tube Robots Based on Actuation Readings Alone

Abdulaziz Y. Alkayas[1,*], Daniel Feliu-Talegon[1], Anup Teejo Mathew[1], Caleb Rucker[2] and Federico Renda[1,3]

Abstract— **Recent advances on Concentric Tube Robots (CTRs) enable the construction and analysis of concentric combinations of precurved elastic tubes. These robots are very appropriate for performing Minimally Invasive Surgery (MIS) with a reduction in patient recovery time. In this work, we propose a kinetostatic model for CTRs based on the Geometric Variable-Strain (GVS) approach where the tubes' sliding motion, the distributed external forces along the tubes and concentrated external forces at the tip, are included. Our approach allows us to estimate the shape of CTRs and the tip forces using the displacements of the tubes and the insertion and rotation input forces and torques. Moreover, we propose a modification in the model, which eliminates completely the sliding friction among the tubes. This new approach opens a new way to use CTRs in surgical applications without the need of sensors along the tubes, but only actuation measurements. The simulation results demonstrate the effectiveness of the proposed approach.**

I. INTRODUCTION

Concentric Tube Robots (CTRs) are considered a class of continuum robots, especially convenient for Minimally Invasive Surgery (MIS). These robots consist of nested, needle-sized, precurved elastic tubes that can rotate and translate relative to each other [1]. These devices are very recommendable for surgical interventions because they can be inserted inside the body through a small incision and perform some kind of inspection or surgery. The relative low invasiveness of these techniques significantly improves the patient recovery. Moreover, the elastic interaction among the tubes provides an infinitive range of shapes and the possibility to control the iteration force between the robot and the environment. These features have recently made CTRs one of the most promising solutions for some surgical interventions [2].

The importance and functionality of these robots have attracted a great interest in the last decades. In particular, the development of CTRs models has driven a fast growth in this field, also leading to numerous problems related with the development of control and sensory systems. Concerning the modelling of CTRs, most of the works found in the literature, develop kinetostatic model based on the equations of Cosserat rods [3], [4]. In these models, the internal bending and torsion of the tubes are described by a set of differential equations and boundary conditions. Moreover, external forces can be added into these models again recalling the Cosserat rod equations [5], [6]. Other works have dealt with the incorporation of the friction forces and torques in the derivation of the models [7], [8], [9]. Subsequently, in [10], the inertial dynamics of a concentric precurved tube system was derived for the first time. This dynamic model deals with any number of tubes with arbitrary precurvature and considers external loading, tube inertia, material damping, Coulomb and viscous friction.

Nowadays there are many techniques that handles the navigation and estimation problems of CTRs. For example in [11], [12], the inverse kinematics is used to compute efficiently the Jacobian for real-time control applications. In [13], nonlinear Model Predictive Control is proposed in order to avoid singular configurations and satisfy mechanical constraints. Also, [14] proposes a task-space position control which is robust to inaccuracies in the kinematic model. Concerning to estimation algorithms of CTRs, some works have developed shape estimators. Shape sensing is necessary for performing path planning [15] and avoid collisions [16]. Thus, in [17], the authors propose a vision based approach for estimating the shape based on X-ray-like images, while [18] predicts the robot's shape by measuring the robot's tip with an electromagnetic sensor together with an accurate model of the CTR. Another interesting work is [19] where a tip position estimation method based on 2D ultrasound images with the help of the forward kinematic model of CTR is proposed. In [20], a purely mechanical approach was introduced for stiffness regulation of CTRs that naturally keeps the tip force within the optimal region of the surgical requirement. Otherwise, force estimation of continuum robots is very useful for applications where the motion of the system is constrained and it is needed a controlled interaction with the environment. Although many works have addressed the force estimation in continuum robots (see for example [21], [22]), very few works have addressed force estimation in CTRs as it is done in [23], or in [24] where a new methodology was proposed to perform force sensing and force control with CTRs.

This work was supported by Khalifa University of Science and Technology under grants CIRA-2020-074 and RC1-2018-KUCARS.

*Corresponding Author: 100052628@ku.ac.ae

[1] Department of Mechanical Engineering, Khalifa Univeristy, Abu Dhabi, UAE

[2] Department of Mechanical, Aerospace and Biomedical Engineering, University of Tennessee, Knoxville, TN 37996, USA

[3] Khalifa University Center for Autonomous Robotic Systems (KU-CARS), Khalifa University, Abu Dhabi, UAE

Email Adresses: 100052628@ku.ac.ae (Abdulaziz Y. Alkayas), daniel.talegon@ku.ac.ae (Daniel Feliu-Talegon), anup.mathew@ku.ac.ae (Anup Teejo Mathew), caleb.rucker@utk.edu (Caleb Rucker), federico.renda@ku.ac.ae (Federico Renda)

Recently, a novel modelling approach has been proposed which is based on a coordinate system which discretizes the continuous Cosserat model of the flexible components onto a finite set of strain basis functions [25], [26]. This Geometric Variable-strain (GVS) approach is a generalization of traditional robotics' geometric model [27] to the case of highly flexible or soft robots [28]. Our previous works [29], [30], use GVS approach to model the equilibrium equations of CTRs relaxing one of the most significant assumptions that were applied in previous works, i.e., quasi-static and time-dependent tubes' sliding. This phenomenon, also know as the sliding spaghetti problem, is intensively studied in the computational mechanics community [31].

In this work, we extend our previous work [29], adding distributed external forces along the tubes (such as gravity) and concentrated external forces at the tip of CTRs, resembling tissue contact. This allows us to estimate the shape and the tip forces using the displacements of the tubes and the insertion and rotation inputs forces and torques, i.e., the actuation readings alone. We also propose a representative scenario where the system is able to estimate some properties of the environment under some relatively mild assumptions. Once, the environment is perceived, our approach allows us to implement a hybrid position/force control based on the inversion of the equilibrium equations. The goal is to present a conceptual methodology for controlling both the position and the contact forces generated at the tip of the CTRs, i.e. the tip can move around the surface [32] while it applies arbitrary forces normal to the surface (force constraint). To the best of the authors' knowledge, this is the first time that the insertion and rotation inputs forces and torques alone are used to estimate the shape and the tip force, simultaneously. This approach opens the possibility to perform surgical interventions without the need to install sensors or cameras along the body of the robot which are not appropriate for the performance of CTRs in real applications [33].

The paper is organized as follows. Section II is devoted to the modelling of the system. Section III presents the shape and force estimation methods. Section IV shows the simulation results of a simulation scenario to demonstrate the advantages of our model and estimators. Finally, some conclusions are given in Section VI.

II. SLIDING CTR MODELLING

In this section we revise and extend the static equilibrium analysis of a sliding-rod variable-strain model for CTRs, introduced in our previous work [29]. External forces are now included, and a reduced formulation is presented that eliminates the need of modeling the sliding friction. To model the system configuration, we use homogeneous transformations. Before going into the details of our CTR system, some preliminaries are defined here. A general space-parametrized (X) homogeneous transformation matrix $\boldsymbol{g}(X) \in SE(3)$ is defined as:

$$\boldsymbol{g}(X) = \begin{pmatrix} \boldsymbol{R}(X) & \boldsymbol{r}(X) \\ \boldsymbol{0}^T & 1 \end{pmatrix}, \tag{1}$$

where, $\boldsymbol{R}(X) \in SO(3)$ is a rotation matrix, and $\boldsymbol{r}(X) \in \mathbb{R}^3$ is the position vector. The time and space derivative of a general homogeneous transformation matrix, $\boldsymbol{g}$, defines the velocity ($\boldsymbol{\eta}$) and strain ($\boldsymbol{\xi}$) twists:

$$\left(\boldsymbol{g}^{-1}(X)\dot{\boldsymbol{g}}(X)\right)^{\vee} = \boldsymbol{\eta}(X) \in \mathbb{R}^6 \tag{2}$$

$$\left(\boldsymbol{g}^{-1}(X)\boldsymbol{g}'(X)\right)^{\vee} = \boldsymbol{\xi}(X) \in \mathbb{R}^6. \tag{3}$$

where, the superscript $\vee$ indicates the isomorphism between the Lie algebra $\mathfrak{se}(3)$ and $\mathbb{R}^6$ ($\wedge$ will be used in the opposite direction) [27].

A. CTR Kinematics

Moving to the specifics of our system, consider the CTR in Figure 1, with an outer tube (tube 1) of length L_1 and an inner tube (tube 2) of length L_2. Both tubes are constrained to be straight before the insertion orifice. We define D_1 and D_2 as the distance from the tube bases to the insertion orifice. Together with D_1 and D_2, the angle of rotation of tube bases α_1 and α_2 constitute the base generalized coordinates of the system $\boldsymbol{q}_b = [D_1, D_2, \alpha_1, \alpha_2]^T$. To model the tubes bases kinematics and from there the rest of the system (as it appears in equation (9)), we fix the spatial frame on the insertion orifice at the end of section 2 and we define $\boldsymbol{g}_t(b,a)$ and $\boldsymbol{g}_r(\theta)$ as:

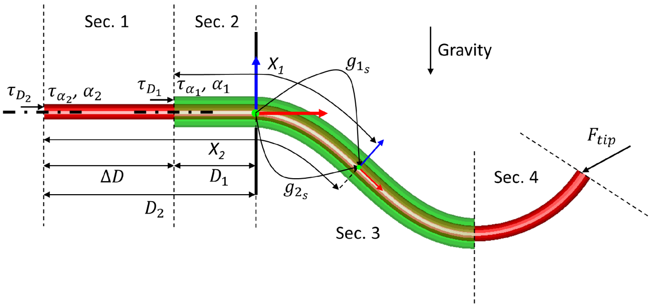

Fig. 1. Schematic of the CTR system. The CTR with the outer tube (tube 1, green) and the inner tube (tube 2, red) is divided into four sections. The red-blue-green arrows indicate coordinate frames, and dot-dash lines indicate the axes of tube rotations. We define the spatial frame at the insertion orifice at the end of section 2. τ_{D_1} and τ_{α_1} are the input force and torque acting at the base of tube 1, while τ_{D_2} and τ_{α_2} correspond to that of tube 2.

$$\boldsymbol{g}_t(b,a) = \begin{pmatrix} \boldsymbol{I} & \boldsymbol{r}_t(b,a) \\ \boldsymbol{0}^T & 1 \end{pmatrix}, \; \boldsymbol{g}_r(\theta) = \begin{pmatrix} \boldsymbol{R}_x(\theta) & \boldsymbol{0} \\ \boldsymbol{0}^T & 1 \end{pmatrix}, \tag{4}$$

where, $\boldsymbol{r}_t(b,a) = [b - a \; 0 \; 0]^T$ and $\boldsymbol{R}_x(\theta)$ is the rotation matrix about the x-axis (the axis tangent to the tubes' midline). The tubes are modeled as inextensible and shearless Cosserat rods (Kirchhoff-Love kinematics) along a material curvilinear abscissa of $X_j \in [0, L_j]$ $(j = 1,2)$ divided into four sections (Figure 1). In the tubes overlapping sections 2 and 3, the abscissas are related by:

$$X_1(\Delta D) = X_2 - \Delta D\,, \tag{5}$$

where, $\Delta D = D_2 - D_1$. For a given tube j and section k, we denote the relative section configuration by, $\boldsymbol{g}_{j,k}(b_{j,k}, a_{j,k})$, where $a_{j,k}$ is the abscissa of tube j at the starting point of section k and $b_{j,k}$ is either X_j or the abscissa of tube j corresponding to the end point of section k. Note that, in general, when we use a subscript of the form 'j,k', j indicates the tube number and k specifies the section number. A further subscript s is used to indicate absolute configurations as opposed to relative ones. The configuration of the inner tube (tube 2) differs from that of the outer tube only by a rotation about the local x-axis of the inner tube. The rotational transformation matrix of tube 2 with respect to the section base is then given by, $\boldsymbol{g}_{\theta_{2,k}}(b_{2,k},a_{2,k})$. $\boldsymbol{g}_{\theta_{2,k}}$ takes the same form of that of $\boldsymbol{g}_r(\theta)$ in equation (4).

We want to represent the configurations of tubes at each sections using strain fields, $\boldsymbol{\xi}_{j,k}$ and $\boldsymbol{\xi}_{\theta_{2,k}}$ [25], where the latter represents the additional torsion of the inner tube. These strain fields are discretized as follows:

$$\boldsymbol{\xi}_{j,k}(X_j) = \boldsymbol{\Phi}_{j,k}(X_j)\boldsymbol{q}_{j,k} + \overline{\boldsymbol{\xi}}\,, \tag{6}$$

$$\boldsymbol{\xi}_{\theta_{2,k}}(X_2) = \boldsymbol{\Phi}_{\theta_{2,k}}(X_2)\boldsymbol{q}_{\theta_{2,k}}\,, \tag{7}$$

where, $\boldsymbol{\Phi}_{j,k}$ and $\boldsymbol{\Phi}_{\theta_{2,k}}$ are basis functions for the respective strain fields, $\boldsymbol{q}_{j,k}$ and $\boldsymbol{q}_{\theta_{2,k}}$ are vectors of generalized coefficients, and $\overline{\boldsymbol{\xi}}$ is equal to $[0\;0\;0\;1\;0\;0]$. Then, the shape generalized coordinates are $\boldsymbol{q}_s = [\boldsymbol{q}_{\theta_{2,1}}^T, \boldsymbol{q}_{1,2}^T, \boldsymbol{q}_{\theta_{2,2}}^T, \boldsymbol{q}_{1,3}^T, \boldsymbol{q}_{\theta_{2,3}}^T, \boldsymbol{q}_{2,4}^T]^T$. We used monomial bases for the strain fields that define the size (n) of the shape generalized coordinates vector. For instance, in section 3 we used:

$$\boldsymbol{\Phi}_{1,3} = \begin{bmatrix} 1 & X_1 & 0 & 0 & 0 & 0 \\ 0 & 0 & 1 & X_1 & 0 & 0 \\ 0 & 0 & 0 & 0 & 1 & X_1 \\ 0 & 0 & 0 & 0 & 0 & 0 \\ 0 & 0 & 0 & 0 & 0 & 0 \\ 0 & 0 & 0 & 0 & 0 & 0 \end{bmatrix}, \quad \boldsymbol{\Phi}_{\theta_{2,3}} = \begin{bmatrix} 1 & X_2 \\ 0 & 0 \\ 0 & 0 \\ 0 & 0 \\ 0 & 0 \\ 0 & 0 \end{bmatrix}. \tag{8}$$

Given that, $\boldsymbol{g}_{j,k}$ and $\boldsymbol{g}_{\theta_{2,k}}$ are computed using equation (3) according to $\boldsymbol{g} = exp(\hat{\boldsymbol{\Omega}})$, where $\boldsymbol{\Omega}(X)$ is the Magnus expansion of the strain field [34]. Putting everything together, the absolute kinematics of the tubes on each section can be written as:

$$\begin{aligned}
&\boldsymbol{g}_{2,1_s}(X_2) = \boldsymbol{g}_t(X_2,D_2)\boldsymbol{g}_r(\alpha_1)\boldsymbol{g}_r(\alpha_2)\boldsymbol{g}_{2,1}(X_2,0) \\[6pt]
&\boldsymbol{g}_{1,2_s}(X_1) = \boldsymbol{g}_t(0,D_1)\boldsymbol{g}_r(\alpha_1)\boldsymbol{g}_{1,2}(X_1,0) \\
&\boldsymbol{g}_{2,2_s}(X_2) = \boldsymbol{g}_{1,2_s}(X_1)\boldsymbol{g}_{\theta_{2,2_s}}(X_2) \\
&\boldsymbol{g}_{\theta_{2,2_s}}(X_2) = \boldsymbol{g}_r(\alpha_2)\boldsymbol{g}_{\theta_{2,1}}(\Delta D,0)\boldsymbol{g}_{\theta_{2,2}}(X_2,\Delta D) \\[6pt]
&\boldsymbol{g}_{1,3_s}(X_1) = \boldsymbol{g}_{1,2_s}(D_1)\boldsymbol{g}_{1,3}(X_1,D_1) \\
&\boldsymbol{g}_{2,3_s}(X_2) = \boldsymbol{g}_{1,3_s}(X_1)\boldsymbol{g}_{\theta_{2,3_s}}(X_2) \\
&\boldsymbol{g}_{\theta_{2,3_s}}(X_2) = \boldsymbol{g}_{\theta_{2,2_s}}(D_2)\boldsymbol{g}_{\theta_{2,3}}(X_2,D_2) \\[6pt]
&\boldsymbol{g}_{2,4_s}(X_2) = \boldsymbol{g}_{2,3_s}(\Delta D+L_1)\boldsymbol{g}_{2,4}(X_2,\Delta D+L_1),
\end{aligned} \tag{9}$$

Moving to differential kinematics, we start with the equality of mixed partial derivatives of $\boldsymbol{g}(X)$. For a transformation matrix of the form, $\boldsymbol{g}(b,a)$, whose boundaries might vary with time due to sliding, the following relation between velocity and strain twist is derived [29]:

$$\boldsymbol{\eta}(b) = \mathrm{Ad}_{\boldsymbol{g}(b)}^{-1}\int_a^b \mathrm{Ad}_{\boldsymbol{g}}\dot{\boldsymbol{\xi}}dX + \boldsymbol{\xi}(b)\dot{b} - \mathrm{Ad}_{\boldsymbol{g}(b)}^{-1}\boldsymbol{\xi}(a)\dot{a}\,, \tag{10}$$

where, the operator Ad is the Adjoint map in $SE(3)$ defined in the Appendix V. Using (10) in the time derivative (2) of the configuration (9), the differential kinematics of each section can be derived [29]:

$$\begin{aligned}
&\boldsymbol{\eta}_{2,1_s}(X_2) = -\overline{\boldsymbol{\xi}}\dot{D}_2 + \boldsymbol{\Phi}_\alpha\dot{\alpha}_1 + \boldsymbol{\Phi}_\alpha\dot{\alpha}_2 + \left(\int_0^{X_2}\boldsymbol{\Phi}_{\theta_{2,1}}dX_2\right)\dot{\boldsymbol{q}}_{\theta_{2,1}} \\[6pt]
&\boldsymbol{\eta}_{1,2_s}(X_1) = -\overline{\boldsymbol{\xi}}\dot{D}_1 + \boldsymbol{\Phi}_\alpha\dot{\alpha}_1 + \left(\int_0^{X_1}\boldsymbol{\Phi}_{1,2}dX_1\right)\dot{\boldsymbol{q}}_{1,2} \\
&\boldsymbol{\eta}_{2,2_s}(X_2) = -\overline{\boldsymbol{\xi}}\dot{D}_2 + \boldsymbol{\Phi}_\alpha\dot{\alpha}_1 + \boldsymbol{\Phi}_\alpha\dot{\alpha}_2 + \left(\int_0^{\Delta D}\boldsymbol{\Phi}_{\theta_{2,1}}dX_2\right)\dot{\boldsymbol{q}}_{\theta_{2,1}} \\
&\quad + \left(\int_0^{X_1}\boldsymbol{\Phi}_{1,2}dX_1\right)\dot{\boldsymbol{q}}_{1,2} + \left(\int_{\Delta D}^{X_2}\boldsymbol{\Phi}_{\theta_{2,2}}dX_2\right)\dot{\boldsymbol{q}}_{\theta_{2,2}} \\[6pt]
&\boldsymbol{\eta}_{1,3_s}(X_1) = \mathrm{Ad}_{\boldsymbol{g}_{1,3}(X_1)}^{-1}\Big[-\bar{\boldsymbol{\xi}}_{k_1}(D_1^+)\dot{D}_1 + \boldsymbol{\Phi}_\alpha\dot{\alpha}_1 + \\
&\quad \left(\int_0^{D_1}\boldsymbol{\Phi}_{1,2}dX_1\right)\dot{\boldsymbol{q}}_{1,2} + \left(\int_{D_1}^{X_1}\mathrm{Ad}_{\boldsymbol{g}_{1,3}(X_1)}\boldsymbol{\Phi}_{1,3}dX_1\right)\dot{\boldsymbol{q}}_{1,3}\Big] \\
&\boldsymbol{\eta}_{2,3_s}(X_2) = \mathrm{Ad}_{\boldsymbol{g}_{\theta_{2,3_s}}(X_2)}^{-1}\boldsymbol{\eta}_{1,3_s}(X_1) - \bar{\boldsymbol{\xi}}_{k_2}(X_2)\Delta\dot{D} + \boldsymbol{\Phi}_\alpha\dot{\alpha}_2 + \\
&\quad \left(\int_0^{\Delta D}\boldsymbol{\Phi}_{\theta_{2,1}}dX_2\right)\dot{\boldsymbol{q}}_{\theta_{2,1}} + \left(\int_{\Delta D}^{D_2}\boldsymbol{\Phi}_{\theta_{2,2}}dX_2\right)\dot{\boldsymbol{q}}_{\theta_{2,2}} + \\
&\quad \left(\int_{D_2}^{X_2}\boldsymbol{\Phi}_{\theta_{2,3}}dX_2\right)\dot{\boldsymbol{q}}_{\theta_{2,3}} \\[6pt]
&\boldsymbol{\eta}_{2,4_s}(X_2) = \mathrm{Ad}_{\boldsymbol{g}_{2,4}(X_2)}^{-1}\Big[\mathrm{Ad}_{\boldsymbol{g}_{\theta_{2,3_s}}(L_1+\Delta D)}^{-1}\boldsymbol{\eta}_{1,3_s}(L_1) - \\
&\quad \bar{\boldsymbol{\xi}}_{k_2}(L_1+\Delta D^+)\Delta\dot{D} + \boldsymbol{\Phi}_\alpha\dot{\alpha}_2 + \left(\int_0^{\Delta D}\boldsymbol{\Phi}_{\theta_{2,1}}dX_2\right)\dot{\boldsymbol{q}}_{\theta_{2,1}} + \\
&\quad \left(\int_{\Delta D}^{D_2}\boldsymbol{\Phi}_{\theta_{2,2}}dX_2\right)\dot{\boldsymbol{q}}_{\theta_{2,2}} + \left(\int_{D_2}^{L_1+\Delta D}\boldsymbol{\Phi}_{\theta_{2,3}}dX_2\right)\dot{\boldsymbol{q}}_{\theta_{2,3}} + \\
&\quad \left(\int_{L_1+\Delta D}^{X_2}\mathrm{Ad}_{\boldsymbol{g}_{2,4}}\boldsymbol{\Phi}_{2,4}dX_2\right)\dot{\boldsymbol{q}}_{2,4}\Big]\,,
\end{aligned} \tag{11}$$

where $\boldsymbol{\Phi}_\alpha = [1\;0\;0\;0\;0\;0]^T$ and $\bar{\boldsymbol{\xi}}_k = [0\;k_y\;k_z\;1\;0\;0]^T$ (k_y and k_z are bending strains). Note that when X_1 appears in the configuration of tube 2, then it become a varying boundary governed by equation (5). Equations (11) provide the Jacobians corresponding to the complete set of $n+4$ generalized coordinates $\boldsymbol{q} = [\boldsymbol{q}_b^T, \boldsymbol{q}_s^T]^T$. It can be seen that there are $N = 6$ sets of Jacobians corresponding to each tube and four sections. We use them to project the static equilibirum equations of the system by d'Alembert's principle [29].

B. CTR Statics

The static equilibirum of a cosserat rod in a concentric tube setting is given by:

$$\mathscr{F}'_{i_j} + \mathrm{ad}^*_{\boldsymbol{\xi}_j}\mathscr{F}_{i_j} + \overline{\mathscr{F}}_{e_j} = \mathbf{0}, \tag{12}$$

where $\mathscr{F}_{i_j}(X) \in \mathbb{R}^6$ is the vector of internal elastic moment and force, $\overline{\mathscr{F}}_{e_j}(X) \in \mathbb{R}^6$ is the vector of distributed external force, and ad^* is the co-adjoint map in $SE(3)$, defined in the Appendix V. Note that we exclude the constraint force due to the concentricity of the tubes by the virtue of the strain parameterization used and the d'Alembert's principle.

Integrating the projected equilibirum equations lead to the final form:

$$\boldsymbol{K}(\boldsymbol{q}) = \boldsymbol{\tau} + \boldsymbol{Q}_e(\boldsymbol{q}), \tag{13}$$

where $\boldsymbol{K}(\boldsymbol{q})$ is the generalized internal elastic force, $\boldsymbol{\tau}$ is the generalized actuation force given by $\boldsymbol{\tau} = [\boldsymbol{\tau}_b^T \ \boldsymbol{0}]^T$, where $\boldsymbol{\tau}_b = [-\tau_{D_1} \ -\tau_{D_2} \ \tau_{\alpha_1} \ \tau_{\alpha_2}]^T$ (indicated in Figure. 1), and $\boldsymbol{Q}_e(\boldsymbol{q})$ is the generalized external force. The expression for $\boldsymbol{K}(\boldsymbol{q})$ is derived in our previous work [29] and can be found in the Appendix V. The generalized external force is given by:

$$\boldsymbol{Q}_e(\boldsymbol{q}) = \sum_{i=1}^{N} \int_{a_i}^{b_i} \boldsymbol{J}_i^T \overline{\mathscr{F}}_{e_i} dX_i + \boldsymbol{J}_6^T(L_2)\mathscr{F}_{tip}, \tag{14}$$

where, $\mathscr{F}_{tip}$ is the tip force $[\boldsymbol{0} \ \boldsymbol{F}_{tip}^T]^T \in \mathbb{R}^6$ expressed in the local coordinate frame and $\overline{\mathscr{F}}_{e_i}$ is the distributed force for instance due to gravity. Equation (13) summarizes all the static equilibrium equations of the system. Note that the first two rows corresponding to D_1 and D_2 are original of this work, and allow the main contribution the manuscript about tip force estimation described in the next sections.

Let us consider the effect of contact friction between the tubes. The contact friction can be modeled as an external force with a sliding force component and a torsional component. As the contact friction acts in equal magnitude and opposite directions between tubes, it is easy to see that the component of sliding fiction cancels out in equation 14 except in the first two rows corresponding to D_1 and D_2. However, summing these two equations, gives

$$\begin{aligned} &\tau_{D_1} + \tau_{D_2} + \left[\bar{\boldsymbol{\xi}}_{k_1}(D_1^+)\right]^T Ad_{\boldsymbol{g}_{1,3}\cdots\boldsymbol{g}_{2,4}}\mathscr{F}_{tip} \\ &= \left(\boldsymbol{\xi}_{k_1}^T\left(\mathscr{F}_{i_1} + \mathrm{Ad}^*_{\boldsymbol{g}_{\theta_{2_s}}}\mathscr{F}_{i_2}\right)\right)(D_2^+) \end{aligned} \tag{15}$$

where $\boldsymbol{\xi}_k = \bar{\boldsymbol{\xi}}_k - \bar{\boldsymbol{\xi}}$, which completely eliminates the component of sliding friction. The torsional friction can be modeled using the Coulomb friction model. However, the torsional friction, which is dependent on the history of tube motion, can be reduced/eliminated by specific actuation histories [35]. Hence, in this paper we do not account for this component.

III. SHAPE AND TIP FORCE ESTIMATION

In this section, we will discuss two main problem formulations for the system of equations (13): the Forward Kinematics Problem (FKP) and the Estimation Problem.

A. Forward Kinematics Problem

The FKP is similar to the forward problem for conventional robots, where the kinematics of each actuator is given to describe the configuration. In the presence of external loads, their reflection on the actuation loads can be also monitored. Similarly, for the case of our CTR system, the base kinematics $\boldsymbol{q}_b$ along with the external tip force $\boldsymbol{F}_{tip}$ (for simplicity we ignore the effects of gravity) can be used to calculate the shape of the CTR $\boldsymbol{q}_s$ and the base actuation load $\boldsymbol{\tau}_b$. For these inputs and outputs, a system of $n+4$ nonlinear equations (13) and $n+4$ unknowns can be solved using a root finding algorithm. We implement the trust-region-dogleg algorithm through the MATLAB function *fsolve* to find a root for this system of equations. Results for the solution of the forward problem can be seen in Table II and Figure 2, where different tip forces were applied showing their effect on the equilibrium configuration and the base actuation load. The physical properties of the studied system is shown in Table I.

TABLE I
PHYSICAL PROPERTIES OF THE STUDIED CTR SYSTEM.

	Tube 1	Tube 2
Young's Modulus (GPa)	58	58
Shear Modulus (GPa)	21.5	21.5
Length (mm)	200	300
Inner Radius (mm)	1.005	0
Outer Radius (mm)	1.195	0.8
Reference Curvature (mm^{-1})	0.1	$0.05 + 0.025X_2$

TABLE II
BASE LOADS FOR DIFFERENT APPLIED TIP FORCES. BASE KINEMATICS FOR ALL CASES ARE: $D_1 = 40\,mm$, $D_2 = 80\,mm$, $\alpha_1 = \alpha_2 = 0\,rad$.

$\boldsymbol{F}_{tip}^T$ (N)	τ_{D_1} (N)	τ_{D_2} (N)	τ_{α_1} (N.m)	τ_{α_2} (N.m)
[0 0 0]	-2.1561	2.1561	0	0
[1.5 0 0]	-5.7139	2.4961	0	0
[0 1 0]	0.2815	-0.6712	0	0
[0 0 -0.5]	-1.6896	1.6704	0.0462	0.0048
[-1 0.5 0]	3.8495	-1.0629	0	0
[0.5 0.5 0.5]	-2.3716	0.9074	-0.0339	-0.0038

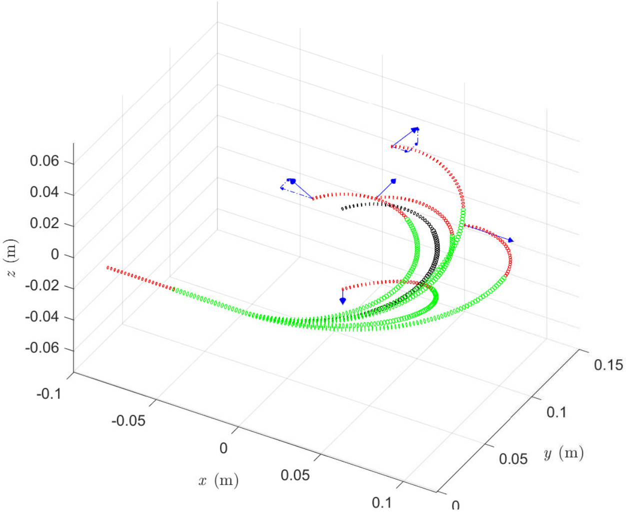

Fig. 2. Configurations of a CTR unloaded (black) and with different tip forces applied (colored). Corresponding base actuation load and kinematics is reported in Table II.

B. Estimation Problem

For the second problem, we leverage the equations that govern the base actuation loads to estimate the applied tip force. The base kinematics $\boldsymbol{q}_b$ and the base actuation load $\boldsymbol{\tau}_b$ are the inputs of the system, and the CTR shape $\boldsymbol{q}_s$ and the tip force $\boldsymbol{F}_{tip}$ are the outputs. The result is an overdetermined system of equations with $n+4$ equations and $n+3$ unknowns. An approximate solution for such system can be achieved through a minimization algorithm. We choose the Levenberg-Marquardt nonlinear least squares algorithm implemented through the MATLAB function *lsqnonlin* to solve the minimization problem defined as:

$$\min_{\boldsymbol{q}_s, \boldsymbol{F}_{tip}} \|\boldsymbol{K}(\boldsymbol{q}) - \boldsymbol{\tau} - \boldsymbol{Q}_e(\boldsymbol{q})\|^2 \tag{16}$$

We demonstrate the estimation performance by applying a random tip force in the range $[-5,\ 5]\,N$ in each direction. We use a linear load ramping technique to properly apply such large-deformation causing loads in the forward problem. Using the resulting $\boldsymbol{\tau}_b$ along with the same $\boldsymbol{q}_b$ used for the forward case, we solve the estimation problem. Fifty out of fifty samples were estimated with negligible error as seen in Figure 3.

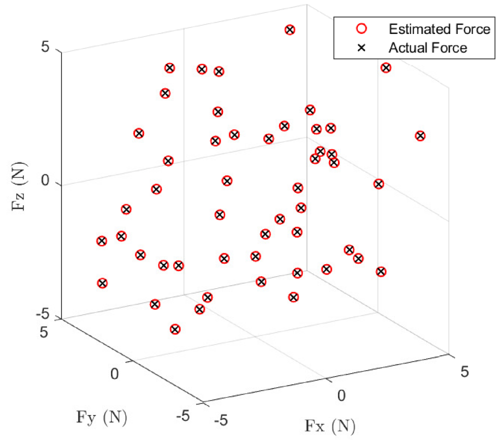

Fig. 3. Estimation performance for 50 samples of the system subject to large deformation-causing tip forces.

For both of the aforementioned problems, we can reap the benefit of adding the first two equations of (13) to implicitly model the sliding friction as discussed in Section II. As a result, the base actuation load vector becomes $\boldsymbol{\tau}_b = [-(\tau_{D_1} + \tau_{D_2}),\ \tau_{\alpha_1},\ \tau_{\alpha_2}]^T \in \mathbb{R}^3$. This reduces by one the number of equations and unknowns for the forward problem, whereas for the estimation problem is only reduced in one the number of equations. This makes that both problems have $n+3$ equations and unknowns which can be solved using root finding problems. However, the main drawback of this method is its heavy dependency on the initial guess for the solution of the estimation problem. It was observed that a same value of $\tau_{D_1} + \tau_{D_2}$ corresponds to multiple shapes and tip force solutions. This phenomenon makes this approach suitable for cases where information about the history of the system development is available like dynamic or quasi-static cases. It will be also tested on a realistic scenario in Section IV, where a proper guess was given only at the beginning of the simulation, and the solution at each step is used as the initial guess for the following step. In this quasi-static simulation, the step size needs to be sufficiently small to ensure proper development of the solution. The step size is experimentally determined through trial and error.

IV. SIMULATED INTERVENTION SCENARIO

In this section, a simulation scenario is conducted in order to show the efficiency of the proposed approach. We show a medical intervention where the CTR navigates inside the body until it achieves a desired part of the body that want to be analysed or healed (dead tissue/tumour). Once the system makes contact with the tissue, it starts a palpation process in order to perceive its properties. Finally, the system performs some kind of treatment or removal of the perceived tissue by following a path with a predefined contact force. Three stages can be differentiated in the proposed application: 1) navigation control (free force motion) of the end-effector of the robot until it makes contact with the tissue, 2) perception of the contact environment and 3) hybrid position/force controller (constrained motion) simulating some kind of surgical application. We assume that the motion is slow enough to make the simulation quasi-static. Inverse kinematics is performed between a set of predefined way-points and the base kinematics are linearly ramped from the current values to the target values. The block diagram for this simulation scenario is shown in Figure 4. A video for the scenario can be viewed in the supplementary material.

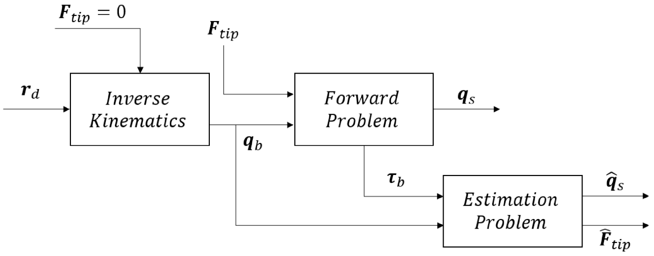

Fig. 4. Block diagram of the proposed simulation scenarios presented in Sections IV-A and IV-B. The diagram also represents the simulation scenario presented in Section IV-C but with a non-zero tip force as an input to the inverse kinematics from the perceived environment model.

We will first formulate the inverse kinematics problem. The inverse kinematics determines the motion of the base kinematics, $\boldsymbol{q}_b$, to reach a desired position with the tip of the robot, $\boldsymbol{r}_{tip}$, under a force at the tip, $\boldsymbol{F}_{tip}$. This problem differs from the ones presented in Section III in that it does not need the equations for the base actuation loads provided that the force at the tip is known. This implies that the system of equations being solved now is (13) excluding the first four rows and adding the tip position constraint equation defined as:

$$\boldsymbol{r}_{tip}(\boldsymbol{q}_b, \boldsymbol{q}_s) - \boldsymbol{r}_d = 0 \tag{17}$$

where $\boldsymbol{r}_d$, $\boldsymbol{r}_{tip}$ is the desired and actual tip position vectors, respectively. $\boldsymbol{r}_{tip}$ is extracted from $\boldsymbol{g}_{tip} = \boldsymbol{g}_{2,4_s}(L_2)$ according to equation 1. As inputs to this problem, we have $\boldsymbol{r}_d$ along with $\boldsymbol{F}_{tip}$, and the solution is $\boldsymbol{q}_s$ and $\boldsymbol{q}_b$. The result is an underdetermined system of equations of $n+3$ equations and $n+4$ unknowns, that can be solved in a similar fashion as the estimation problem.

A. Navigation control in free motion

During free motion, the CTR is not exchanging forces with the environment. Then, the inverse kinematics is performed for the tip position considering that the tip force is zero, $\boldsymbol{F}_{tip} = \mathbf{0}$. This allows for any desired navigation of the CTR tip. In Figure 5, the navigation phase is represented (solid black curve) where the CTR enters the body through an insertion incision (red circle) and starts following a specific tip trajectory. At every step, the tip force acting on the CTR is estimated. Contact with the environment is detected when the magnitude of this estimation is higher than a predefined threshold. We set this threshold to be higher than the maximum force estimate in free motion to avoid numerical inaccuracies (near zero estimations) being detected as contact.

B. Estimators based on actuation readings

Once the contact is detected, we propose to perceive the environment with our approach. In the proposed scenario, we assume that the environment that we want to identify is a spherical body of an unknown radius and with a force field that grows inversely with the distance from the center. This force field is defined using an n^{th} order polynomial. Then, the force at the tip of the robot, $\boldsymbol{F}_{tip}(\boldsymbol{r}_{tip})$, contacting with the environment can be defined in function of the tip position $\boldsymbol{r}_{tip}$, as follows:

$$D = ||\boldsymbol{r}_{tip} - \boldsymbol{r}_c||, \tag{18}$$

$$P_n(s) = \sum_{i=1}^{n} a_i s^i, \tag{19}$$

$$\boldsymbol{F}_{tip}(\boldsymbol{r}_{tip}) = \begin{cases} 0 & \text{if } D > R_s \\ P_n(R_s - D)\dfrac{\boldsymbol{r}_{tip} - \boldsymbol{r}_c}{D} & \text{if } D < R_s \end{cases}, \tag{20}$$

where D is the distance from the center, $\boldsymbol{r_c}$ is the position of the center of the sphere, R_s is the sphere radius and a_i are the polynomial coefficients that describe the force field. We choose an n^{th} order polynomial because any function can be approximated through Taylor series of infinite number of terms. We perform unconstrained inverse kinematics to palpate the soft body. It is done between each of the predefined waypoints. For i waypoints we have $\boldsymbol{q}_{b_i}$, then motion is achieved by linear interpolation between each corresponding element in $\boldsymbol{q}_{b_i}$ and $\boldsymbol{q}_{b_{i+1}}$ into a specific number of steps. In every step, we estimate the force at the tip by solving the estimation problem as shown in Figure 4. Due to the unmodelled tip force in the inverse kinematics, a mismatch may arise between the desired and actual tip positions. However, that should not pose any concern as the primary target is just to palpate the soft body. In the forward problem, the tip force of the concentric tube robot in contact with the environment is calculated from equation (20) where the direction is pointing out the sphere in the radial direction. That defines a new variant for the FKP where the applied tip force is model-based rather than arbitrarily given. Under these assumptions, the following methodology to perceive the environment is proposed:

1) Center: Radial parameterized lines, $\boldsymbol{p}_i = \boldsymbol{r}_{tip,i} + t\frac{\boldsymbol{F}_{tip,i}}{||\boldsymbol{F}_{tip,i}||}$, are reconstructed through the current contact point and the direction of the estimated force vector. Let two reconstructed radial lines be $\boldsymbol{p}_1$ and $\boldsymbol{p}_2$, the center of the sphere is defined by the intersection of these lines.
2) Force field: Solving the minimization problem defined as:

$$\min_{a_i, R_s} \sum_{j=1}^{k} \left(||\boldsymbol{F}_{tip,j} - \hat{\boldsymbol{F}}_j||\right)^2, \tag{21}$$

where $\hat{\boldsymbol{F}}_j$ is the j^{th} recorded estimated force , and $\boldsymbol{F}_{tip,j}$ is the the force from the proposed force model (20), the estimation of the coefficients of the force field, $\hat{a}_i$, and the radius of the sphere $\hat{R}_s$ are obtained.

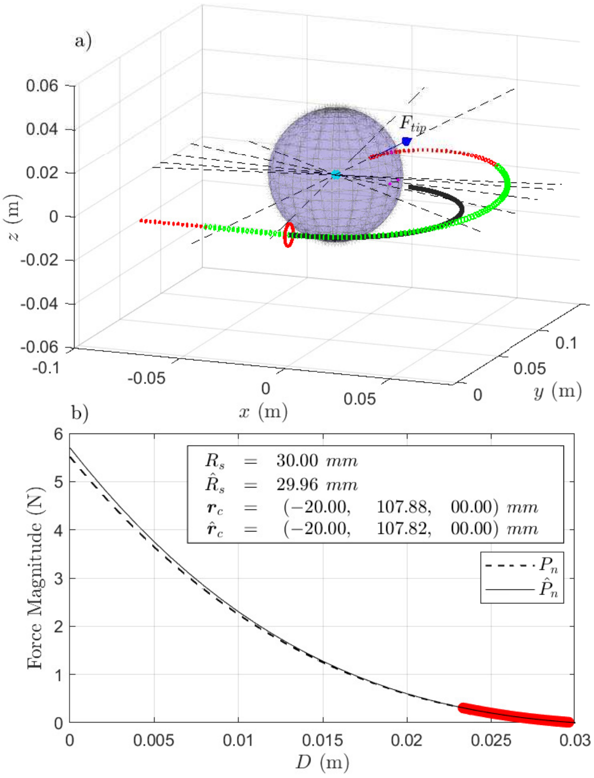

Fig. 5. (a) The CTR at the end of the sensing scenario touching the identified soft sphere. Dashed lines (black) indicate the reconstructed radial lines to estimate the sphere center (cyan). The free motion navigation path is shown as the solid thick line (black) from the insertion incision (red circle) to the close vicinity of the soft sphere. (b) The final estimation results for the sphere center, radius and stiffness.

A snapshot from the end of the sensing scenario can be seen in Figure 5 where all the parameters of the soft body were estimated with a small error. For this simulation, we choose the variants for the forward and estimation problems with the added base load equations (15). We choose a polynomial of 3^{rd} order to define the force field with the coefficients $a_0 = 0$, $a_1 = 25$, $a_2 = 2500$, $a_3 = 10^5$. The estimated coefficients are $\hat{a}_0 = -9.17 \times 10^{-4}$, $\hat{a}_1 = 25.54$, $\hat{a}_2 = 2484.2$, $\hat{a}_3 = 0.844 \times 10^5$.

C. Hybrid position/force control in constrained motion

Once the environment is estimated, we can use our approach to implement a hybrid position/force control emulating some kind of surgical applications. Here, the position around a surface (tissue) is controlled while a force normal to this surface is applied. In contrast to the inverse kinematics performed in section IV-A where the applied tip force was zero, the information from the estimated environment along with equation (17) can be used to perform constrained inverse kinematics. This additional information is used to compensate for any mismatch in the tip position due to the constrained motion and allows us to perform hybrid position/force control for the CTR. We demonstrate this by following a trajectory at a constant distance from the center of the sphere. The trajectory is a projected ellipse on a sphere of radius 25 *mm* with the center at $\hat{\boldsymbol{r}}_c$. Results for the tracking performance is presented in Figure 6.

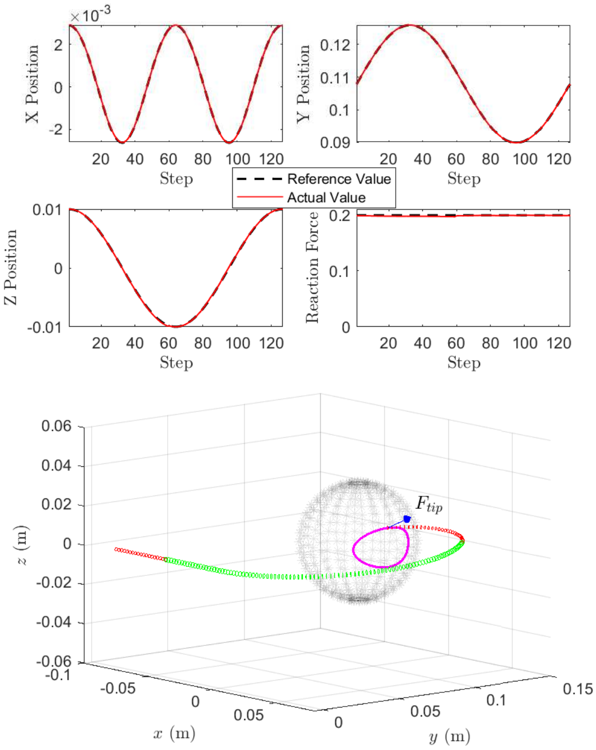

Fig. 6. Trajectory following results for the hybrid position/force control after the estimation of the soft body parameters. The Root Mean Squared Error (RMSE) for each value is as follows: $RMSE_x = 0.0154$ *mm*, $RMSE_y = 0.0239$ *mm*, $RMSE_z = 0.0694$ *mm*, $RMSE_{||\boldsymbol{F}_{tip}||} = 0.0019$ *N*.

V. CONCLUSIONS

In this paper, we utilized the actuation measurements of a CTR system to perform model-based shape and tip force estimation. Unlike other techniques, our approach does not rely on body integrated sensors. Somehow, it reminds us of conventional robot systems where only the loads at the actuators can be used to estimate external loads. Simulations show the capability of our approach to estimate large deformation-causing tip forces with high accuracy. We have also proposed a modification to the model that completely eliminates the sliding friction between the tubes. We present with a realistic scenario the effectiveness of this new approach. Simulations demonstrate free motion, environment perception, and accurate hybrid position/force control. As future work, we aim to design and fabricate an experimental CTR prototype having minimal friction and base load measurement capabilities, allowing for experimental -alongside numerical- validation of the proposed approach.

APPENDIX

$$
\begin{aligned}
K(D_1) = {} & EI_{x_1}\left[\left(\boldsymbol{\xi}_{k_1}^T\left(\boldsymbol{\xi}_{k_1}-\boldsymbol{\xi}_{k_1}^*\right)\right)(D_1^+)\right] + EI_{x_2}\left[\frac{1}{2}\left(\boldsymbol{\xi}_{k_1}^T\boldsymbol{\xi}_{k_1}\right)(D_2^+) + \right. \\
& \int_{D_2}^{L_1+\Delta D}\left(\boldsymbol{\xi}_{k_1}' + \mathrm{ad}_{\boldsymbol{\xi}_1}\bar{\boldsymbol{\xi}}_{k_1}\right)^T \mathrm{Ad}_{\boldsymbol{g}_{\theta_{2s}}}\boldsymbol{\xi}_{k_2}^* dX + \\
& \left(\boldsymbol{\xi}_{k_1}^T\left(\frac{1}{2}\boldsymbol{\xi}_{k_1} - \mathrm{Ad}_{\boldsymbol{g}_{\theta_{2s}}}\boldsymbol{\xi}_{k_2}^*\right)\right)(L_1+\Delta D^-) - \\
& \left.\left(\boldsymbol{\xi}_{k_2}^T\left(\boldsymbol{\xi}_{k_2}-\boldsymbol{\xi}_{k_2}^*\right)\right)(L_1+\Delta D^+)\right] \\
K(D_2) = {} & EI_{x_2}\left[\left(\boldsymbol{\xi}_{k_1}^T\left(\frac{1}{2}\boldsymbol{\xi}_{k_1} - \mathrm{Ad}_{\boldsymbol{g}_{\theta_{2s}}}\boldsymbol{\xi}_{k_2}^*\right)\right)(D_2^+) - \right. \\
& \int_{D_2}^{L_1+\Delta D}\left(\boldsymbol{\xi}_{k_1}' + \mathrm{ad}_{\boldsymbol{\xi}_1}\bar{\boldsymbol{\xi}}_{k_1}\right)^T \mathrm{Ad}_{\boldsymbol{g}_{\theta_{2s}}}\boldsymbol{\xi}_{k_2}^* dX - \\
& \left(\boldsymbol{\xi}_{k_1}^T\left(\frac{1}{2}\boldsymbol{\xi}_{k_1} - \mathrm{Ad}_{\boldsymbol{g}_{\theta_{2s}}}\boldsymbol{\xi}_{k_2}^*\right)\right)(L_1+\Delta D^-) + \\
& \left.\left(\boldsymbol{\xi}_{k_2}^T\left(\boldsymbol{\xi}_{k_2}-\boldsymbol{\xi}_{k_2}^*\right)\right)(L_1+\Delta D^+)\right] \\
K(\alpha_1) = {} & \boldsymbol{\Phi}_\alpha^T \int_{D_2}^{L_1+\Delta D} \mathrm{ad}_{\boldsymbol{\xi}_1}^* \mathrm{Ad}_{\boldsymbol{g}_{\theta_{2s}}}^* \mathscr{F}_{i_2} dX \\
K(\alpha_2) = {} & -\boldsymbol{\Phi}_\alpha^T \int_{D_2}^{L_1+\Delta D} \mathrm{ad}_{\boldsymbol{\xi}_1}^* \mathrm{Ad}_{\boldsymbol{g}_{\theta_{2s}}}^* \mathscr{F}_{i_2} dX \\
\boldsymbol{K}(\boldsymbol{p}_{\theta_{2,1}}) = {} & \int_0^{\Delta D} \boldsymbol{\Phi}_{\theta_{2,1}}^T \mathscr{F}_{i_2} dX - \boldsymbol{J}_{\theta_{2,1}}^T(\Delta D)\int_{D_2}^{\Delta D+L_1} \mathrm{ad}_{\boldsymbol{\xi}_1}^* \mathrm{Ad}_{\boldsymbol{g}_{\theta_{2s}}}^* \mathscr{F}_{i_2} dX \\
\boldsymbol{K}(\boldsymbol{p}_{1,2}) = {} & \int_{\Delta D}^{D_2} \boldsymbol{\Phi}_{1,2}^T\left(\mathscr{F}_{i_1} + \mathscr{F}_{i_2}\right) dX \\
\boldsymbol{K}(\boldsymbol{p}_{\theta_{2,2}}) = {} & \int_{\Delta D}^{D_2} \boldsymbol{\Phi}_{\theta_{2,2}}^T \mathscr{F}_{i_2} dX - \boldsymbol{J}_{\theta_{2,2}}^T(D_2)\int_{D_2}^{\Delta D+L_1} \mathrm{ad}_{\boldsymbol{\xi}_1}^* \mathrm{Ad}_{\boldsymbol{g}_{\theta_{2s}}}^* \mathscr{F}_{i_2} dX \\
\boldsymbol{K}(\boldsymbol{p}_{1,3}) = {} & \int_{D_2}^{\Delta D+L_1} \boldsymbol{\Phi}_{1,3}^T\left(\mathscr{F}_{i_1} + \mathrm{Ad}_{\boldsymbol{g}_{\theta_{2s}}}^* \mathscr{F}_{i_2}\right) dX \\
\boldsymbol{K}(\boldsymbol{p}_{\theta_{2,3}}) = {} & \int_{D_2}^{\Delta D+L_1} \boldsymbol{\Phi}_{\theta_{2,3}}^T \mathscr{F}_{i_2} dX - \int_{D_2}^{\Delta D+L_1} \boldsymbol{J}_{\theta_{2,3}}^T \mathrm{ad}_{\boldsymbol{\xi}_1}^* \mathrm{Ad}_{\boldsymbol{g}_{\theta_{2s}}}^* \mathscr{F}_{i_2} dX \\
\boldsymbol{K}(\boldsymbol{p}_{2,4}) = {} & \int_{\Delta D+L_1}^{L_2} \boldsymbol{\Phi}_{2,4}^T \mathscr{F}_{i_2} dX
\end{aligned}
$$

where, E is the Young's modulus and I_x is the polar moment of inertia of tubes.

$$
\mathrm{Ad}_{\boldsymbol{g}} = \begin{pmatrix} \boldsymbol{R} & \mathbf{0}_{3\times3} \\ \widetilde{\mathbf{r}}\boldsymbol{R} & \boldsymbol{R} \end{pmatrix}, \mathrm{Ad}_{\boldsymbol{g}}^* = \begin{pmatrix} \boldsymbol{R} & \widetilde{\mathbf{r}}\boldsymbol{R} \\ \mathbf{0}_{3\times3} & \boldsymbol{R} \end{pmatrix},
$$

$$
\mathrm{ad}_{\boldsymbol{\xi}} = \begin{pmatrix} \widetilde{\mathsf{k}} & \mathbf{0}_{3\times3} \\ \widetilde{\mathsf{u}} & \widetilde{\mathsf{k}} \end{pmatrix}, \mathrm{ad}_{\boldsymbol{\xi}}^* = \begin{pmatrix} \widetilde{\mathsf{k}} & \widetilde{\mathsf{u}} \\ \mathbf{0}_{3\times3} & \widetilde{\mathsf{k}} \end{pmatrix}
$$

REFERENCES

[1] H. B. Gilbert, D. C. Rucker, and R. J. Webster III, "Concentric tube robots: The state of the art and future directions," *Robotics Research*, pp. 253–269, 2016.

[2] H. Alfalahi, F. Renda, and C. Stefanini, "Concentric tube robots for minimally invasive surgery: Current applications and future opportunities," *IEEE Transactions on Medical Robotics and Bionics*, vol. 2, no. 3, pp. 410–424, 2020.

[3] D. C. Rucker, R. J. Webster III, G. S. Chirikjian, and N. J. Cowan, "Equilibrium conformations of concentric-tube continuum robots," *The International journal of robotics research*, vol. 29, no. 10, pp. 1263–1280, 2010.

[4] P. E. Dupont, J. Lock, B. Itkowitz, and E. Butler, "Design and control of concentric-tube robots," *IEEE Transactions on Robotics*, vol. 26, no. 2, pp. 209–225, 2009.

[5] D. C. Rucker, B. A. Jones, and R. J. Webster III, "A geometrically exact model for externally loaded concentric-tube continuum robots," *IEEE transactions on robotics*, vol. 26, no. 5, pp. 769–780, 2010.

[6] J. Lock, G. Laing, M. Mahvash, and P. E. Dupont, "Quasistatic modeling of concentric tube robots with external loads," in *2010 IEEE/RSJ international conference on intelligent robots and systems*, pp. 2325–2332, IEEE, 2010.

[7] J. Ha and P. E. Dupont, "Incorporating tube-to-tube clearances in the kinematics of concentric tube robots," in *2017 IEEE International Conference on Robotics and Automation (ICRA)*, pp. 6730–6736, IEEE, 2017.

[8] J. Ha, G. Fagogenis, and P. E. Dupont, "Modeling tube clearance and bounding the effect of friction in concentric tube robot kinematics," *IEEE Transactions on Robotics*, vol. 35, no. 2, pp. 353–370, 2018.

[9] J. Lock and P. Dupont, "Friction modeling in concentric tube robots," *IEEE International Conference on Robotics and Automation : ICRA : [proceedings] IEEE International Conference on Robotics and Automation*, pp. 1139–1146, 05 2011.

[10] J. Till, V. Aloi, K. E. Riojas, P. L. Anderson, R. J. Webster III, and C. Rucker, "A dynamic model for concentric tube robots," *IEEE Transactions on Robotics*, vol. 36, no. 6, pp. 1704–1718, 2020.

[11] K. Leibrandt, C. Bergeles, and G.-Z. Yang, "On-line collision-free inverse kinematics with frictional active constraints for effective control of unstable concentric tube robots," in *2015 IEEE/RSJ International Conference on Intelligent Robots and Systems (IROS)*, pp. 3797–3804, IEEE, 2015.

[12] J. Burgner, D. C. Rucker, H. B. Gilbert, P. J. Swaney, P. T. Russell, K. D. Weaver, and R. J. Webster, "A telerobotic system for transnasal surgery," *IEEE/ASME Transactions on Mechatronics*, vol. 19, no. 3, pp. 996–1006, 2013.

[13] M. Khadem, J. O'Neill, Z. Mitros, L. Da Cruz, and C. Bergeles, "Autonomous steering of concentric tube robots via nonlinear model predictive control," *IEEE Transactions on Robotics*, vol. 36, no. 5, pp. 1595–1602, 2020.

[14] M. N. Boushaki, C. Liu, and P. Poignet, "Task-space position control of concentric-tube robot with inaccurate kinematics using approximate jacobian," in *2014 IEEE International Conference on Robotics and Automation (ICRA)*, pp. 5877–5882, IEEE, 2014.

[15] L. G. Torres, C. Baykal, and R. Alterovitz, "Interactive-rate motion planning for concentric tube robots," in *2014 IEEE International Conference on Robotics and Automation (ICRA)*, pp. 1915–1921, IEEE, 2014.

[16] A. Bajo and N. Simaan, "Kinematics-based detection and localization of contacts along multisegment continuum robots," *IEEE Transactions on Robotics*, vol. 28, no. 2, pp. 291–302, 2011.

[17] A. Vandini, C. Bergeles, B. Glocker, P. Giataganas, and G.-Z. Yang, "Unified tracking and shape estimation for concentric tube robots," *IEEE Transactions on Robotics*, vol. 33, no. 4, pp. 901–915, 2017.

[18] E. Mackute, B. Thamo, K. Dhaliwal, and M. Khadem, "Shape estimation of concentric tube robots using single point position measurement,"

[19] Z. Li, X. Yang, S. Song, L. Liu, and M. Q.-H. Meng, "Tip estimation approach for concentric tube robots using 2d ultrasound images and kinematic model," *Medical & Biological Engineering & Computing*, vol. 59, no. 7, pp. 1461–1473, 2021.

[20] H. Alfalahi, F. Renda, C. Messer, and C. Stefanini, "Exploiting the instability of eccentric tube robots for distal force control in minimally invasive cardiac ablation," *Proceedings of the Institution of Mechanical Engineers, Part C: Journal of Mechanical Engineering Science*, vol. 235, no. 23, pp. 7212–7232, 2021.

[21] D. C. Rucker and R. J. Webster, "Deflection-based force sensing for continuum robots: A probabilistic approach," in *2011 IEEE/RSJ International Conference on Intelligent Robots and Systems*, pp. 3764–3769, IEEE, 2011.

[22] M. A. Diezinger, B. Tamadazte, and G. J. Laurent, "3d curvature-based tip load estimation for continuum robots," *IEEE Robotics and Automation Letters*, vol. 7, no. 4, pp. 10526–10533, 2022.

[23] H. Donat, S. Lilge, J. Burgner-Kahrs, and J. J. Steil, "Estimating tip contact forces for concentric tube continuum robots based on backbone deflection," *IEEE Transactions on Medical Robotics and Bionics*, vol. 2, no. 4, pp. 619–630, 2020.

[24] M. Mahvash and P. Dupont, "Stiffness control of continuum surgical manipulators," *IEEE Trans. Robotics*, vol. 27, no. 2, pp. 334–345, 2011.

[25] F. Renda, C. Armanini, V. Lebastard, F. Candelier, and F. Boyer, "A geometric variable-strain approach for static modeling of soft manipulators with tendon and fluidic actuation," *IEEE Robotics and Automation Letters*, vol. 5, no. 3, pp. 4006–4013, 2020.

[26] F. Boyer, V. Lebastard, F. Candelier, and F. Renda, "Dynamics of continuum and soft robots: A strain parameterization based approach," *IEEE Transactions on Robotics*, vol. 37, no. 3, pp. 847–863, 2021.

[27] R. Murray, Z. Li, and S. Sastry, *A Mathematical Introduction to Robotic Manipulation*. Taylor & Francis, Boca Raton, USA, 1994.

[28] F. Renda and L. Seneviratne, "A geometric and unified approach for modeling soft-rigid multi-body systems with lumped and distributed degrees of freedom," in *2018 IEEE International Conference on Robotics and Automation (ICRA)*, pp. 1567–1574, IEEE, 2018.

[29] F. Renda, C. Messer, C. Rucker, and F. Boyer, "A sliding-rod variable-strain model for concentric tube robots," *IEEE Robotics and Automation Letters*, vol. 6, no. 2, pp. 3451–3458, 2021.

[30] F. Boyer, V. Lebastard, F. Candelier, and F. Renda, "Extended hamilton's principle applied to geometrically exact kirchhoff sliding rods," *Journal of Sound and Vibration*, vol. 516, p. 116511, 2022.

[31] A. Humer, I. Steinbrecher, and L. Vu-Quoc, "General sliding-beam formulation: A non-material description for analysis of sliding structures and axially moving beams," *Journal of Sound and Vibration*, vol. 480, p. 115341, 2020.

[32] M. C. Yip, J. A. Sganga, and D. B. Camarillo, "Autonomous control of continuum robot manipulators for complex cardiac ablation tasks," *Journal of Medical Robotics Research*, vol. 2, no. 01, p. 1750002, 2017.

[33] Z. Mitros, S. H. Sadati, R. Henry, L. Da Cruz, and C. Bergeles, "From theoretical work to clinical translation: Progress in concentric tube robots," *Annual Review of Control, Robotics, and Autonomous Systems*, vol. 5, pp. 335–359, 2022.

[34] A. T. Mathew, I. M. B. Hmida, C. Armanini, F. Boyer, and F. Renda, "Sorosim: A matlab toolbox for hybrid rigid-soft robots based on the geometric variable-strain approach," *IEEE Robotics and Automation Magazine*, pp. 2–18, 2022.

[35] J. Ha, G. Fagogenis, and P. E. Dupont, "Modeling tube clearance and bounding the effect of friction in concentric tube robot kinematics," *IEEE Transactions on Robotics*, vol. 35, no. 2, pp. 353–370, 2019.